RSC Advances

PAPER

View Article Online
View Journal | View Issue

Cite this: *RSC Adv.*, 2017, **7**, 5473

Three-dimensional inkjet-printed redox cycling sensor†

N. Y. Adly,[a] B. Bachmann,[b] K. J. Krause,[a] A. Offenhäusser,[a] B. Wolfrum[ab] and A. Yakushenko*[a]

Received 22nd November 2016
Accepted 31st December 2016

DOI: 10.1039/c6ra27170g

www.rsc.org/advances

Multilayer inkjet printing is emerging as a robust platform for fabricating flexible electronic devices over a large area. Here, we report a straightforward, scalable and inexpensive method for printing multilayer three-dimensional nanoporous redox cycling devices with a tunable nanometer gap for electrochemical sensing. The fabrication of the electrochemical redox cycling device is based on vertical stacking of two conductive electrodes made of carbon and gold nanoparticle inks. In this configuration, the two electrodes are parallel to each other and electrically separated by a layer of polystyrene nanospheres. As the top and the bottom electrodes are biased to, respectively, oxidizing and reducing potentials, repetitive cycling of redox molecules between them generates a large current amplification. We show that a vertical interelectrode spacing down to several hundred nanometers with high precision using inkjet printing is possible. The printed sensors demonstrate excellent performance in electrochemical sensing of ferrocene dimethanol as a redox-active probe. A collection efficiency of 100% and current amplification up to 30-fold could be obtained. Our method provides a low cost and versatile means for sensitive electrochemical measurements eliminating the need for sophisticated fabrication methods, which could prove useful for sensitive point-of-care diagnostics devices.

Introduction

Redox cycling at the nanoscale is a highly sensitive method for electrochemical detection of redox-active analytes.[1–7] The method relies on amplification of Faradic currents due to recurrent oxidation and reduction of redox-active molecules between two closely spaced and independently biased electrodes. The amplified current provides quantitative information on the concentration of the redox-active molecules allowing direct detection of analytes at low concentrations.[8,9] The distance between the two electrodes plays a significant role here, as the amplified current inversely scales with the interelectrode distance. Recently, the Lemay group has demonstrated single-molecule resolution, the ultimate level of detection, using microfabricated nanofluidic redox cycling devices.[9–11] Since the introduction of redox cycling devices in electrochemistry,[12] a variety of electrode configurations has been studied. Apart from probe-based techniques, such as scanning electrochemical microscopy,[13,14] most investigations have been performed using interdigitated electrodes (IDE) with a narrow interelectrode distance.[5,15–19] However, the minimal distance between the anode and the cathode is limited by the lateral resolution of the fabrication process. Thus, advanced lithographic techniques are required to fabricate efficient redox cycling devices at the nanoscale using IDE configuration. An alternative to the lateral configuration is a multi-layer vertical electrode arrangement. Here, two electrodes are aligned on top of each other and are separated by a thin sacrificial layer, which is etched away in a post-processing step to form a nanogap. In this configuration, the thickness of the sacrificial layer will determine the distance between the two electrodes. Conceptually, this design has the advantage of allowing the realization of a defined gap between the electrodes down to the nanometer range.[20,21] Another interesting approach is redox cycling in nanoporous devices.[22–29] These sensors are based on metal/insulator/metal stack with pores created on the top electrode and the insulator layer allowing the diffusion of analyte solution to the bottom electrode through the pores offering a high temporal resolution for electrokinetic studies. Yet, all of the aforementioned designs utilize rather expensive state-of-the-art microfabrication techniques. If redox cycling devices are going to be applied in areas requiring low cost of production, such as point-of-care testing, alternative fabrication methods have to be considered. Recently, Park *et al.*[30] have demonstrated a benchtop fabrication of a redox cycling sensor of vertically stacked electrodes using 0.54 to 8 μm beads as a spacer. However, their

[a]*Institute of Bioelectronics (PGI-8/ICS-8), JARA—Fundamentals of Future Information Technology, Forschungszentrum Jülich, 52425 Jülich, Germany. E-mail: A.Yakushenko@fz-juelich.de*

[b]*Neuroelectronics, MSB, Department of Electrical and Computer Engineering, Technical University of Munich (TUM) & BCCN Munich, Boltzmannstrasse 11, Garching, 85748 Germany*

† Electronic supplementary information (ESI) available. See DOI: 10.1039/c6ra27170g

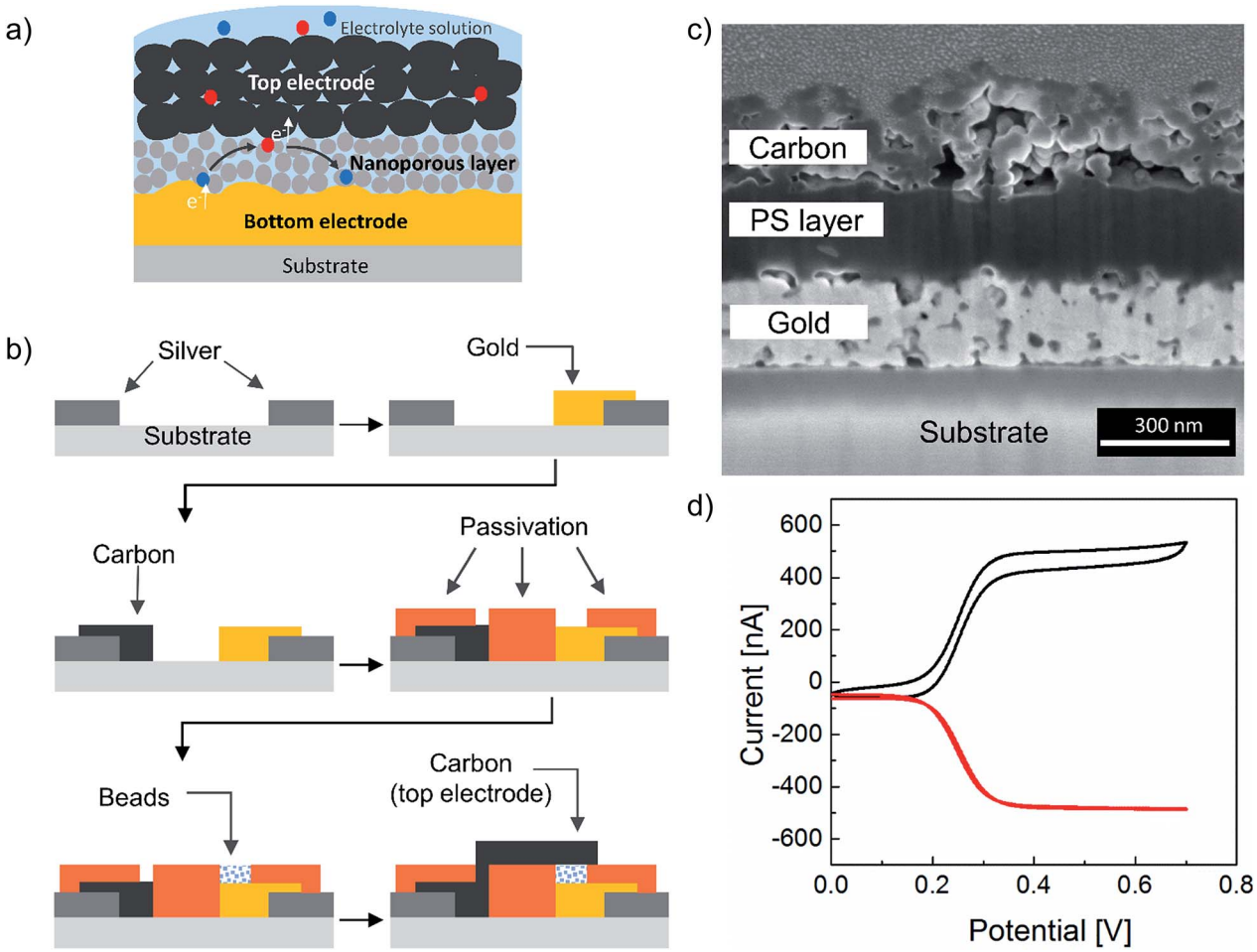

Fig. 1 (a) The principle of redox cycling in a nanoporous device: reduced species (blue circles) is first oxidized at the top electrode (red circles) and then diffuses through the pores of the polystyrene layer to be re-reduced at the bottom electrode (blue circles). Thereafter, the process is repeated until the molecule escapes the device. (b) Schematic illustration of the fabrication flow of the redox cycling sensor. (c) Cross-sectional SEM image of the printed device (d) the measured cyclic voltammograms recorded at the carbon top electrode (black curve) and at the bottom gold electrode (red curve) with 500 μM $Fc(MeOH)_2$. The potential of the bottom electrode was held at 0.0 V while the top electrode was swept from 0.0 V to 0.6 V at a scan rate of 20 mV s^{-1}.

method involves several substrate treatment steps and most importantly a manual assembly of two separated electrode plates, which is a very tedious and time-consuming, and therefore, an unscalable procedure. On the other hand, additive manufacturing methods such as inkjet printing offer a practical solution to cost and scalability problems.[31,32] Although lateral resolution in ink-jet printing is limited by the smallest drop size to approximately 10–20 μm,[31–33] if Z resolution of inkjet printing is exploited, vertical interelectrode spacing down to several hundred nanometers is feasible. Here, for the first time, we present an array of fully printed three-dimensional redox cycling sensors using multiple functional inks. Neither substrate pre-treatment nor post-possessing beyond sintering were used during fabrication since the inks inherently possessed all the required functionality. We used inkjet printing for fabricating a vertically stacked redox cycling device using carbon and gold nanoparticle inks. Each printed chip has material costs of less than 5 cents (see Table S1†). At the same time, we combined a novel nanoporous material made of layers of polystyrene nanospheres for electrical isolation between the two electrodes. As schematically illustrated in Fig. 1a, the redox cycling device consists of a porous top carbon electrode, which allows the transport of the electrolyte solution to the bottom electrode. The bottom electrode (made either of gold or carbon nanoparticle inks) is separated by a nanoporous layer, thereby allowing the diffusion of redox molecules between the two electrodes. The entire device was passivated with a dielectric ink as described in the experimental section, leaving only the sensor area (three layer system described above) exposed to the electrolyte.

We performed a proof-of-principle demonstration of a redox cycling device using a gold nanoparticle ink as a bottom electrode material. Further experiments were carried out using carbon bottom and top electrodes instead of gold for three key reasons: (a) carbon is a cheaper alternative to noble metals; (b) the use of carbon in electrochemistry has been and continues to be of great interest across a wide range of applications due to its wider potential window compared to gold (see Fig. S1†); (c) the

use of carbon-based materials in cleanroom technology still poses a technical challenge, although carbon electrodes are ubiquitous in cutting-edge platforms such as supercapacitors, fuel cells, and bioelectronics.[33]

The results presented here involve the use of printed microelectrodes (ME) as the sensing electrode. As opposed to macroelectrodes, ME feature a three-dimensional diffusion field, which leads to a steady-state current, and faster electron transfer due to smaller size and lower capacitance values, which in turn leads to enhanced sensitivity.[34,35] Microelectrode array systems have been reported in literature for the single-molecule detection and single-molecule electrocatalysis owing to their inherent advantages.[36,37]

Results and discussion

Printing process

The printing process is shown in Fig. 1b. Silver nanoparticle ink was first deposited on a polyethylene naphthalate (PEN) substrate forming the feedlines for electrical connections followed by either a gold or carbon ink deposition for the active bottom electrode. Both inks were prepared as described in the experimental section. Afterward, a dielectric polyimide ink was used to passivate the electrodes and define an electrode opening as shown on the microscopic image of the fabrication sequence in Fig. S2.† As a next step, a polystyrene nanosphere ink was printed onto the bottom electrode. This layer was crucial in providing mechanical stability to the next deposited layer. Upon drying of the polystyrene nanosphere layer, a carbon top electrode was printed on top of it. Finally, the entire sensor was cured using photonic sintering to sinter the upper carbon layer without damaging the polystyrene nanospheres. An additional potential advantage of using a polystyrene nanosphere ink is the possibility to later utilize carboxyl or amine functionalization to bind a biorecognition element such as DNA or protein for sensing applications. Another feature of this approach, namely using a nanoporous dielectric layer, is the elimination of the sacrificial layer and with it of the post-etching step, which is typical in the fabrication of two superimposed electrodes. Fig. 1c shows a cross-sectional view obtained from Focused Ion Beam (FIB) milling of the device. Approximately 280 nm separation between the top and the bottom electrodes can be observed as three layers of polystyrene nanospheres were printed. This demonstrates the ability to print a multilayer stack of four different material inks with high precision. Fig. 1d demonstrates successful utilization of the fabricated device for sensing of ferrocene dimethanol as a redox-active probe. Here, the top anode is providing the oxidizing potential to the redox molecules as it is being swept from negative to positive potentials, while the bottom cathode collects and reduces all the molecules that have been previously oxidized at the top anode and diffused to the cathode. This is evident from the collection efficiency that is close to 100% in our device. The collection efficiency η is defined by the ratio of

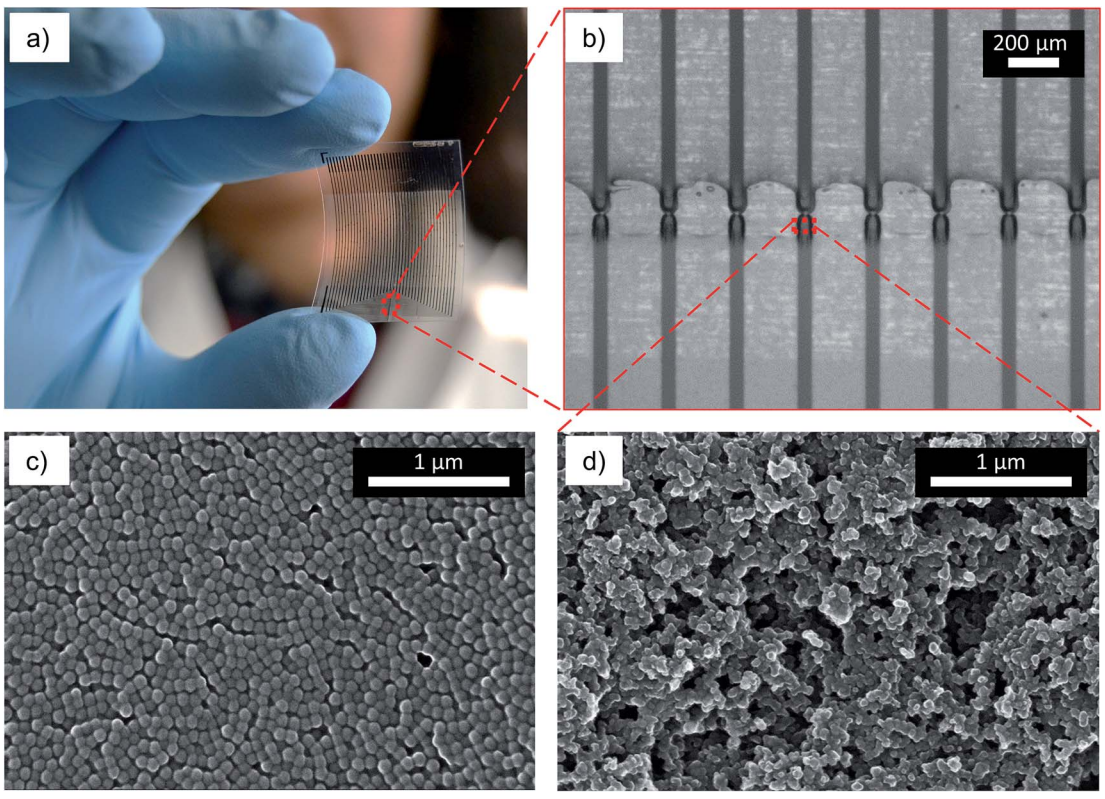

Fig. 2 Large scale inkjet printing of vertically stacked redox cycling sensors: (a) optical image of inkjet-printed redox cycling device on a flexible substrate. (b) Microscopic image of a printed carbon electrode (c) and (d) SEM images of printed polystyrene nanospheres and carbon, respectively.

the current for reduced species at the bottom electrode divided by the current for the oxidation of reduced species at the top electrode, see eqn (1).[38,39]

$$\eta = \frac{I_{(\text{bottom})}}{I_{(\text{top})}} \quad (1)$$

A camera image of the fabricated redox cycling chip is shown in Fig. 2a. Each chip consists of 25 sensors (50 feedlines) printed using silver and carbon inks on PEN substrates. The width and length of each bottom carbon electrode were 45 μm and 60 μm, respectively, as seen in Fig. 2b. The top electrodes were arranged above the bottom electrode having a width of ~220 μm and a length of ~145 μm. The complete fabrication steps are depicted in the ESI.† The repeatability of the process in lateral resolution is in the range of 4%. Fig. 2c shows the nanoporous layer of as-printed polystyrene nanospheres. The surface morphology and the porosity of the printed carbon electrode are evident from the high magnification SEM image in Fig. 2d.

The thickness of the polystyrene film critically depends on the number of printed layers. Although a small distance of 200 nm between the top and the bottom electrodes was possible as seen in Fig. 2c, we printed arrays of redox cycling sensors with a 1200 nm distance. We did that in order to increase the yield of functional devices by avoiding possible failures due to short circuits and to ensure higher mechanical stability of the top carbon electrode. This larger distance between the two electrodes was achieved by printing 12 layers of polystyrene nanospheres. Consequently, this interelectrode distance d defines the amplification. It should be noted that the redox cycling current scales with $1/d$ for vertical gap devices.[36] In the case of a nanoporous gap, additional obstacles to the diffusion of redox molecules are introduced. Therefore, we further characterized the sensors as shown in the electrochemical results in Fig. 3 using an all-carbon printed device. To test the sensitivity of our devices, we constructed an electrochemical calibration curve with varying concentrations of ferrocene dimethanol as shown in part (a) and (b) of Fig. 3. Fig. 3b shows the dependence of the oxidation current at the top electrode on the concentration of the redox molecules. The response was linear ($R^2 = 0.98$) over a range of 250 μM to 1 μM for the top electrode, as shown in Fig. 3b.

As mentioned earlier, obstacles due to the presence of the polystyrene nanospheres between the oxidizing and the reducing electrodes will affect the amplified current, which is expected to be smaller than in a hollow gap device of the same size. The redox cycling current I can be calculated by eqn (2) and (3).[10]

$$N_{\text{molecule}} \frac{De}{h^2} \quad (2)$$

$$N_{\text{molecule}} = N_{\text{A}} V C_0 \quad (3)$$

where N_{A} is the Avogadro's number, V is the free volume between the two electrodes, C_0 is the bulk concentration of ferrocene dimethanol, D is the diffusion coefficient of ferrocene dimethanol, e is elementary charge and h is the distance between the two electrodes. The free volume can be calculated from the active area of 45 μm × 60 μm, where top and bottom electrodes overlap, and a 1200 nm spacing between the two electrodes.

Assuming a ferrocene dimethanol concentration of 250 μM with a diffusion coefficient of 6.7×10^{-10} m^2 s^{-1} this would result in a redox cycling current of 36.4 nA. This value is only valid for a free volume between the electrodes. Here, the free volume is reduced by the spacing layer of polystyrene nanospheres. Additionally, the actual length of the diffusive pathway will increase due to the hindered diffusion within the nanoporous layer. If we now, for example, assume a hexagonal dense packing of polystyrene nanospheres, this would reduce the free volume by 74% and elongate the pathway by at least 20% resulting in a suppressed redox cycling current of 6.6 nA. The measured current (Fig. 3b) during redox cycling mode was 2.9

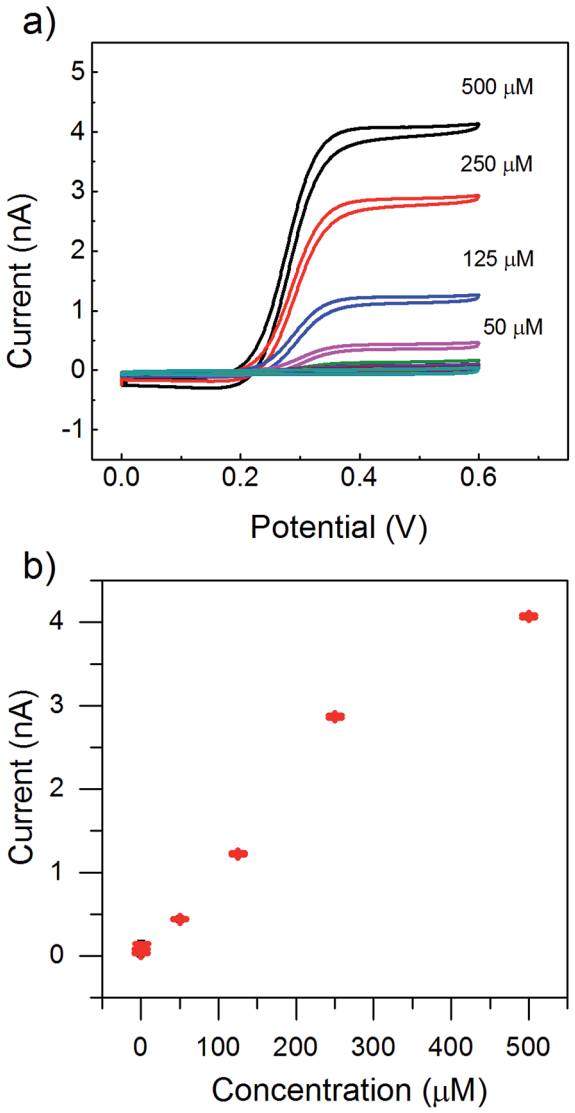

Fig. 3 (a) Redox cycling current measured for the top electrode at different concentrations of ferrocene dimethanol; the scan rate at the bottom electrode was 20 mV s^{-1}. (b) Limiting currents obtained from voltammograms of ferrocene dimethanol at the top electrode as a function of concentration. Error bars show standard deviation of three cycles.

nA, which is of the same order of magnitude as the expected current calculated by these very basic assumptions. We attributed the deviation to the difference between the geometrical area and the active electrochemical area of the electrodes.

Overall, the printed device showed an enhancement in the overall current values of the mostly reduced ferrocene dimethanol redox species, which was about 30 times higher with the redox cycling mode on compared to the mode when the top anode was inactive. We found that the sensitivities of the top and the bottom electrodes were 3.1×10^3 A $(m^2\ M)^{-1}$ and 5.9×10^3 A $(m^2\ M)^{-1}$, respectively. We were able to distinguish concentrations down to 1 nM, however, the linear slope of these values differed from the one for the higher concentration range. Further investigation is required to explore these discrepancies.

In order to demonstrate the stability of the sensor during long electrochemical measurements, we performed a cyclability test by continuously cycling the top electrode while biasing the bottom electrode. The redox cycling current was measured for a random device over thirty cycles at a slow scan rate of 20 mV s^{-1} in a 500 μM ferrocene dimethanol solution in PBS. As seen in Fig. S3,† the current remained almost constant for around 30 cycles, after which degradation started. This relative long-term stability shows a potential for a broad range of applications, which require prolonged or multiple measurements. Furthermore, the chemo-mechanical stability of the vertically stacked electrodes was also evaluated based on the change in redox cycling current in a vigorously stirred PBS solution. We found a negligible change in the current before and after immersing the chip in PBS as shown in Fig. S4.†

Experimental

Materials

Nano-silver ink (DGP 40LT-15C) was bought from Advanced Nano Products, Co., Ltd, South Korea. PEN foil (Optfine® PQA1M) from Teijin DuPont Films was used as a flexible substrate for inkjet printing. All ink jetting experiments were performed using an OmniJet 300 inkjet printer, UniJet Co., Republic of Korea, with 1 or 10 pL DMC cartridges from Fujifilm Dimatix Inc., USA. The sintering and curing steps were conducted on a precision hot plate (CT10, Harry Gestigkeit GmbH, Germany). Prior to printing, all inks were sonicated in a sonication bath for 5 minutes and filtered with 0.45 μm syringe filter.

Preparation of the carbon ink

1 g of carbon black (Orion Carbons) in 5 g of a 50/50 wt% mixture of ethylene glycol and water were milled with 100 μm yttrium zirconium beads at 1100 rpm for 1 hour in a Pulverisette 7 ball mill (Fritsch, Germany). The milled mass was diluted with further 10 g of ethylene glycol/water mixture to adjust the viscosity with vigorous stirring. The solution was filtered through a 0.45 μm filter to obtain the final ink.

Preparation of the gold ink

Hexanethiol-capped gold nanoparticles were prepared using Brust–Shiffrin synthesis as described in other works.[44,45] The as-prepared gold nanoparticles were dissolved at a concentration of 20 wt% in a 30/70 wt% mixture of toluene and a-terpineol to obtain a jettable viscosity. The solution was filtered through a 0.45 μm filter to obtain the final ink.

Fabrication of fully printed redox cycling sensors arrays

The overall process flow for the fabrication of the redox cycling sensor is illustrated in Fig. 1a. First, silver nanoparticle ink was printed with a drop spacing of 22 μm, frequency of 2 kHz and a substrate temperature of 50 °C. Next, carbon nanoparticle ink was patterned on top of the silver ink using a 22 μm drop spacing, a frequency of 1 kHz and a substrate temperature of 25 °C. Next, the printed arrays were sintered at 120 °C for 30 minutes. After printing the carbon and the silver arrays, tuning the surface energy of the PEN substrate (PQA1M) for printing a dielectric layer of polyimide ink was carried out by exposing the whole substrate to oxygen plasma in a plasma oven (Nano, Diener Electronic, Germany) at a power of 30 W and pressure of 0.2 mbar for 12 seconds. Subsequently, the electrode insulation was created by printing the polyimide polymer with a drop spacing of 25 μm and frequency of 5 kHz. Upon printing, the passivation ink was cured thermally by heating to 80 °C on a hot plate for 5 minutes followed by 120 °C for 30 minutes.

Patterning of a nanoporous layer using polystyrene nanospheres

The colloidal ink of polystyrene nanospheres consisted of 40 wt% polystyrene nanospheres (mean diameter of 120 nm), 50 wt% dipropylene glycol and 10 wt% deionized water (from a Millipore Milli-Q system, 18 Ω cm^{-1}). Next, the colloidal ink was sonicated in an ultrasonic bath for 15 minutes. Later, the nanoparticle solution was deposited on top of the previously printed carbon electrode using a 10 pL cartridge while the substrate temperature was set to 60 °C. In order to vary the thickness of the nanoporous layer, several printing passes using the polystyrene ink were performed.

Top electrode fabrication

The carbon top electrode was aligned and deposited on top of the printed nonporous layer as shown in the schematic in Fig. 1b. In order to mechanically stabilize the top electrode, each sample was flash-annealed by a photonic curing system (PulseForge 1200, NovaCentrix, USA) with six 500 μs long pulses of 200 V (fluence of 0.296 J cm^{-2} as measured using an integrated bolometer) with a flashing frequency of 1 Hz.

Characterization

SEM images were taken with a Nova Nano (FEI, USA) scanning electron microscope (SEM) with an accelerating voltage of 5 kV. Cross-sectional images and FIB cuts were performed by a Helios Nanolab 600i apparatus (FEI, USA). After depositing a protective 500 nm platinum layer, the milling and the polishing were carried on using an ion voltage of 30 kV and current of 80 pA. The printed nanoporous layer thickness was also measured using a surface profiler (DEKTAK 3030).

Chip design layout

The multi-electrode microchip consisted of 50 silver/carbon electrodes/feedlines (inner diameter: 35 ± 4 μm; center to center spacing: 205 ± 5 μm). The size of the printed chip as shown in Fig. 2a was 20 mm × 30 mm. It could be inserted into a 50-pin FPC connector with top contact flip-lock type, the contact pads have a 0.5 mm pitch. Each chip consists 50 feedlines. The width and length of each bottom carbon electrode were 45 μm and 60 μm, respectively, the top electrodes were arranged above the bottom electrode having a width of ~220 μm and a length of ~145 μm.

Electrochemical measurements of the printed sensors

All electrochemical measurements were carried out using CHI Instruments (CHI1030B, CH Instruments Inc., USA) and employing an Ag/AgCl reference electrode (Super Dri-ref SDR 2, World Precision Instruments, USA). Measurements of redox-active molecules were done by preparing a solution of 1,1-ferrocene dimethanol (Sigma-Aldrich) in PBS (pH 7.4). Redox cycling was carried out by fixing the bottom electrodes at a constant potential (0.0 V). The top electrode was swept from 0.0 V to 0.6 V at a scan rate of 20 mV s^{-1}. Therefore, the redox molecules underwent repetitive oxidation and reduction *via* continuous diffusion from one electrode to another before eventually escaping the device and diffusing away into the bulk solution through the porous top electrode. The reducing and oxidizing currents were measured independently. Stability study was done by placing the whole chip in a 250 mL beaker filled with 100 with PBS solution and applying stirring conditions by rotating a 2.5 mm magnetic stirrer bar at 400 rpm.

Electrical characterization

The resistance of the printed test structures was measured after sintering and flash-curing using a multimeter (Voltcraft Plus VC 960, Conrad, Germany). The calculated resistivity of printed silver and carbon layers was found to be 6.4×10^{-8} Ω m and 1.05×10^{-2} Ω m, respectively.

Conclusion

In summary, we report a straightforward, scalable and inexpensive method for fabricating three-dimensional nanoporous redox cycling devices with a tunable nanometer gap for electrochemical redox cycling sensing. The separation between the two electrodes is controlled primarily by the number of the polystyrene nanosphere layers. Subsequently, different gap sizes down to hundred nanometers and up to several micrometers can be realized. In contrast to the present state-of-the-art, no cleanroom facilities are required to fabricate such a highly sensitive sensing device. This method enables the fabrication of multiple devices on large-area substrates and completely eliminates the post-processing steps apart from curing. We are currently extending the method to incorporate a biorecognition element into the nanoporous layer directly *via* a biomodified polystyrene nanosphere ink. In addition, we believe that three-dimensional inkjet printing of two conductive electrodes with a tunable nanometer to micrometer separation could also be applied beyond electrochemical sensing, for example for high-energy storage devices such as supercapacitors.[40–49]

Acknowledgements

We would like to acknowledge the financial support from Helmholtz Validation Fund within the project HVF-0034 "Live-Check" and the Helmholtz Young Investigators Program. We would also like to thank Elke Brauweiler-Reuters for SEM and FIB images.

References

1 O. Niwa, Y. Xu, H. B. Halsall and W. R. Heineman, *Anal. Chem.*, 1993, **65**, 1559–1563.
2 Y. Kanno, K. Ino, H. Shiku and T. Matsue, *Lab Chip*, 2015, **15**, 4404–4414.
3 N. Alayo, C. Fernández-Sánchez, A. Baldi, J. P. Esquivel, X. Borrisé and F. Pérez-Murano, *Microchim. Acta*, 2016, **183**, 1633–1639.
4 K. Ino, T. Nishijo, Y. Kanno, H. Shiku and T. Matsue, *ECS Trans.*, 2013, **50**, 205–210.
5 V. a. T. Dam, W. Olthuis and A. van den Berg, *Analyst*, 2007, **132**, 365–370.
6 J. L. Hammond, A. J. Gross, P. Estrela, J. Iniesta, S. J. Green, C. P. Winlove, P. G. Winyard, N. Benjamin and F. Marken, *Anal. Chem.*, 2014, **86**, 6748–6752.
7 H. M. Harvey, A. J. Gross, P. Brooksby, A. J. Downard, S. J. Green, C. P. Winlove, N. Benjamin, P. G. Winyard, M. Whiteman, J. L. Hammond, P. Estrela and F. Marken, *Electroanalysis*, 2015, **27**, 2645–2653.
8 W. R. Vandaveer IV, D. J. Woodward and I. Fritsch, *Electrochim. Acta*, 2003, **48**, 3341–3348.
9 S. G. Lemay, S. Kang, K. Mathwig and P. S. Singh, *Acc. Chem. Res.*, 2013, **46**, 369–377.
10 M. A. G. Zevenbergen, P. S. Singh, E. D. Goluch, B. L. Wolfrum and S. G. Lemay, *Nano Lett.*, 2011, **11**, 2881–2886.
11 P. S. Singh, E. Kätelhön, K. Mathwig, B. Wolfrum and S. G. Lemay, *ACS Nano*, 2012, **6**, 9662–9671.
12 L. B. Anderson and C. N. Reilley, *J. Electroanal. Chem.*, 1965, **10**, 295–305.
13 R. C. Engstrom, M. Weber, D. J. Wunder, R. Burgess and S. Winquist, *Anal. Chem.*, 1986, **58**, 844–848.
14 A. J. Bard, F. R. F. Fan, J. Kwak and O. Lev, *Anal. Chem.*, 1989, **61**, 132–138.
15 K. Ueno, M. Hayashida, J.-Y. Ye and H. Misawa, *Electrochem. Commun.*, 2005, **7**, 161–165.
16 D. G. Sanderson and L. B. Anderson, *Anal. Chem.*, 1985, **57**, 2388–2393.
17 M. Morita, K. Hayashi, T. Horiuchi, S. Shibano, K. Yamamoto and K. J. Aoki, *J. Electrochem. Soc.*, 2014, **161**, H178–H182.
18 R. Kamath and M. J. Madou, *ECS Trans.*, 2014, **61**, 65–73.
19 Y. Kanno, T. Goto, K. Ino, K. Y. Inoue, Y. Takahashi, H. Shiku and T. Matsue, *Anal. Sci.*, 2014, **30**, 305–309.

20 B. Wolfrum, M. Zevenbergen and S. Lemay, *Anal. Chem.*, 2008, **80**, 972–977.
21 E. Kätelhön, B. Hofmann, S. G. Lemay, M. A. Zevenbergen, A. Offenhäusser and B. Wolfrum, *Anal. Chem.*, 2010, **82**, 8502–8509.
22 L. P. Zaino, C. Ma and P. W. Bohn, *Microchim. Acta*, 2016, **183**, 1019–1032.
23 C. Ma, N. M. Contento, L. R. Gibson and P. W. Bohn, *ACS Nano*, 2013, **7**, 5483–5490.
24 M. Hüske, R. Stockmann, A. Offenhäusser and B. Wolfrum, *Nanoscale*, 2014, **6**, 589–598.
25 D.-H. Han, L. P. Zaino, K. Fu and P. W. Bohn, *J. Phys. Chem. C*, 2016, **120**(37), 20634–20641.
26 M. Hüske, R. Stockmann, A. Offenhäusser and B. Wolfrum, *Nanoscale*, 2013, **6**, 589–598.
27 C. Ma, W. Xu, W. R. A. Wichert and P. W. Bohn, *ACS Nano*, 2016, **10**, 3658–3664.
28 S. Neugebauer, U. Müller, T. Lohmüller, J. P. Spatz, M. Stelzle and W. Schuhmann, *Electroanalysis*, 2006, **18**, 1929–1936.
29 T. Lohmüller, U. Müller, S. Breisch, W. Nisch, R. Rudorf, W. Schuhmann, S. Neugebauer, M. Kaczor, S. Linke, S. Lechner, J. Spatz and M. Stelzle, *J. Micromech. Microeng.*, 2008, **18**, 115011.
30 S. Park, J. H. Park, S. Hwang and J. Kwak, *Electrochem. Commun.*, 2016, **68**, 76–80.
31 V. Subramanian, J. B. Chang, A. de la Fuente Vornbrock, D. C. Huang, L. Jagannathan, F. Liao, B. Mattis, S. Molesa, D. R. Redinger, D. Soltman, S. K. Volkman and Q. Zhang, in *Solid-State Circuits Conference, 2008. ESSCIRC 2008. 34th European*, 2008, pp. 17–24.
32 V. Subramanian, P. C. Chang, J. B. Lee, S. E. Molesa and S. K. Volkman, *IEEE Trans. Compon. Packag. Technol.*, 2005, **28**, 742–747.
33 M. Singh, H. M. Haverinen, P. Dhagat and G. E. Jabbour, *Adv. Mater.*, 2010, **22**, 673–685.
34 D. A. Walsh, K. R. J. Lovelock and P. Licence, *Chem. Soc. Rev.*, 2010, **39**, 4185.
35 A. Bard, A. Boika, S. Kwon, J. Park and S. Thorgaard, in *Nanoelectrochemistry*, CRC Press, 2015, pp. 241–292.
36 J. E. Dick, C. Renault and A. J. Bard, *J. Am. Chem. Soc.*, 2015, **137**, 8376–8379.
37 A. N. Sekretaryova, M. Y. Vagin, A. P. F. Turner and M. Eriksson, *J. Am. Chem. Soc.*, 2016, **138**, 2504–2507.
38 A. J. Bard, J. A. Crayston, G. P. Kittlesen, T. Varco Shea and M. S. Wrighton, *Anal. Chem.*, 1986, **58**, 2321–2331.
39 E. Kätelhön and B. Wolfrum, *Rev. Anal. Chem.*, 2012, **31**, 7–14.
40 M. A. G. Zevenbergen, B. L. Wolfrum, E. D. Goluch, P. S. Singh and S. G. Lemay, *J. Am. Chem. Soc.*, 2009, **131**, 11471–11477.
41 M. J. Hostetler, J. E. Wingate, C. J. Zhong, J. E. Harris, R. W. Vachet, M. R. Clark, J. D. Londono, S. J. Green, J. J. Stokes, G. D. Wignall, G. L. Glish, M. D. Porter, N. D. Evans and R. W. Murray, *Langmuir*, 1998, **14**, 17–30.
42 P. Ihalainen, H. Majumdar, T. Viitala, B. Törngren, T. Närjeoja, A. Määttänen, J. Sarfraz, H. Härmä, M. Yliperttula, R. Österbacka and J. Peltonen, *Biosensors*, 2012, **3**, 1–17.
43 G. Cai, P. Darmawan, M. Cui, J. Wang, J. Chen, S. Magdassi and P. S. Lee, *Adv. Energy Mater.*, 2016, **6**, DOI: 10.1002/aenm.201670025.
44 Y. Xu, I. Hennig, D. Freyberg, A. James Strudwick, M. Georg Schwab, T. Weitz and K. Chih-Pei Cha, *J. Power Sources*, 2014, **248**, 483–488.
45 S. H. Ko, H. Pan, C. P. Grigoropoulos, C. K. Luscombe, J. M. J. Fréchet and D. Poulikakos, *Nanotechnology*, 2007, **18**, 345202.
46 B. S. Cook, J. R. Cooper and M. M. Tentzeris, *IEEE Microw. Wirel. Compon. Lett.*, 2013, **23**, 353–355.
47 C. J. Curtis, M. V. Hest, A. Miedaner, T. Kaydanova, L. Smith and D. S. Ginley, in *2006 IEEE 4th World Conference on Photovoltaic Energy Conference*, 2006, vol. 2, pp. 1392–1394.
48 L. Hu, H. Wu and Y. Cui, *Appl. Phys. Lett.*, 2010, **96**, 183502.
49 D. Pech, M. Brunet, P.-L. Taberna, P. Simon, N. Fabre, F. Mesnilgrente, V. Conédéra and H. Durou, *J. Power Sources*, 2010, **195**, 1266–1269.